Journal of Applied Fluid Mechanics, Vol. 19, No. 4, pp. 723-737, 2026.
Available online at www.jafmonline.net, ISSN 1735-3572, EISSN 1735-3645.
https://doi.org/10.47176/jafm.19.4.3953

Coupled Fluid–structure Interaction Simulation of Aerodynamic Load Fluctuations and Fatigue Life in a Centrifugal Fan FN280

N. Aimeur†, A. Amour, and N. Menasri

Laboratory of Materials and Structural Mechanics, University of Mohamed BoudiafM'sila, B.P 166 Ichbilia, M'sila, 28000, Algeria

†*Corresponding Author Email: noureddine.aimeur@univ-msila.dz*

ABSTRACT

Rotating machinery such as centrifugal fans is often exposed to unsteady aerodynamic loads that can induce fatigue damage during prolonged industrial operation. This study investigates the fatigue life of a centrifugal fan (FN280) used in a cement plant through a one-way fluid–structure interaction (FSI) approach. Transient aerodynamic loads were computed using ANSYS Fluent and subsequently transferred to ANSYS Mechanical for structural fatigue analysis. Since the original fan geometry was unavailable, a detailed three-dimensional model was reconstructed via reverse engineering to ensure accurate aerodynamic representation. The unsteady numerical simulations were performed under four operating conditions and validated against experimental performance data. The comparison shows a satisfactory level of agreement, confirming the reliability of the adopted modelling approach. Simulation results indicate that most regions of the fan exhibit fatigue safety factors between 1 and 15, suggesting generally safe operation. However, localized stress concentrations near the blade root and shaft–disc junction display safety factors slightly below unity, indicating potential sites for early fatigue crack initiation. The estimated fatigue life is approximately 2.8×10^6 cycles, emphasizing the significance of accounting for aerodynamic loading effects in fatigue assessment. Overall, the study demonstrates the capability of FSI-based numerical simulations for predictive maintenance and reliability evaluation, while further experimental validation is recommended.

Article History

Received August 26, 2025
Revised October 24, 20xx
Accepted November 6, 2025
Available online February 5, 2026

Keywords:

Computational fluid dynamics (CFD)
Fluid–structure interaction Coupled one-way
Finite Element Analysis (FEA)
Fatigue
Reverse engineering
Centrifugal fan

1. INTRODUCTION

In the design of rotating machinery, controlling rotor vibrations is essential, as excessive vibration can lead to failure through instability or fatigue. Fatigue is one of the important domains of research in this field, especially since rotating machines such as turbines and centrifugal fans are regularly exposed to fluid flows. The passage of fluid through these machines causes pressure fluctuations, which in turn generate variable loads that affect their service life (Choi et al., 2003; Wolfram & Carolus, 2010).

These machines are widely used in various industrial processes, where operational reliability is critical to prevent costly downtime. In cement production plants, for instance, centrifugal fans are subjected to turbulent airflow, which can lead to excessive vibrations and fatigue-related failures. Despite their widespread use, the influence of turbulent flow characteristics on the fatigue behavior and service life of these fans remains insufficiently understood, emphasizing the need for continued research in this area.

Over the past years, numerous studies have been conducted to understand the effect of vibrations on the performance of centrifugal fans, which pose a technical challenge impacting operational efficiency and performance stability. In this context, Nan et al. (2024b) showed that the installation angle of stationary blades in gas turbine compressors directly affects the dynamic forces generated on the rotating blades, causing vibrations that lead to changes in the blades 'dynamic response and a reduction in their lifespan due to cyclic fatigue, particularly in the blade root regions, which are subjected to high dynamic stresses.

In line with this, the study conducted by Zhou et al., (2023) investigated the flow-induced vibration of a centrifugal pump under the effect of stator–rotor interaction using a one-way FSI approach. Their results revealed that the blade passing frequency and the shaft

NOMENCLATURE

$\Omega_f(t)_s$	fluid domain at time t	ρ_f	fluid density
$\Omega_s(t)$	solid domain at time t	μ_f	fluid dynamic viscosity
$\Gamma_{fs}(t)$	fluid–structure interface	u	solid displacement vector
n_f	unit outward normal vector on the fluid side	$\dot{u}$	solid velocity vector
n_s	unit outward normal vector on the solid side $(n_s = -n_f)$	$\ddot{u}$	solid acceleration vector
v	fluid velocity vector	ρ_s	solid density
p	fluid pressure	σ_f	fluid Cauchy stress tensor
f	body force per unit mass	σ_s	solid Cauchy stress tensor
ε	strain tensor in the solid	E	Young's modulus of the solid
v	Poisson's ratio of the solid	λ, μ	Lamé parameters
I	second-order identity tensor	S	fluid rate-of-strain tensor

rotational frequency are the main characteristic frequencies responsible for pressure pulsations and dynamic responses in the pump. Furthermore, the study by Zhou et al. (2025) addressed the response of centrifugal fan arms, analyzing vibration modes and resonance at maximum operating speeds. Multi-objective optimization methods were employed to reduce peak vibration speed and minimize resonance risks, thereby enhancing structural reliability and overall fan performance.

In a related context, other studies have examined the effect of turbulent airflow and the resulting dynamic loads on the performance of centrifugal fans, as well as their connection to vibrations and mechanical failure. For example, Fakhfekh et al. (2025) demonstrated that rotor blade flexibility in a turbulent flow environment leads to bending and twisting deformations that alter flow patterns and wake vortices, which in turn affect aerodynamic forces such as lift, drag, and thrust, thereby influencing the overall performance of the fan. Dadhich et al. (2015) noted that fans, during operation particularly in start-up and shutdown phases are subjected to centrifugal, bending, and vibrational loads. The repetition of these leads to increased cyclic stress and eventual failure of fan components, making in essential to conduct precise analyses to avoid resonance phenomena that could exacerbate the damage.

Dadhich et al. (2015) demonstrated that changing the inlet closure level causes variations in both static and dynamic pressure inside the fan casing, leading to increased turbulence intensity and vibrations, which in turn affect service life and performance efficiency.

Moreover, numerous studies have addressed the impact of airflow, as well as various operational and design factors, on the performance of centrifugal fans and their relationship to vibrations, noise, and mechanical failure (Alphin et al., 2025; Danilishin et al., 2020; He et al., 2021; Liu & Liu, 2024; More et al., 2020; Ottersten et al., 2022; Wei et al., 2022).

Amid these complexities, the field of FSI analysis has witnessed significant advancements, becoming an essential tool for understanding the intricate relationship between flow and structural analysis to comprehensively assess the effect of aerodynamic loads on structural response.

For example, Li et al. (2023) applied FSI analysis to study fan deformations resulting from flow-structure interactions, as in molten salt pumps, while Zhang et al., (2020) used two-way FSI analysis to investigate the effect of unsteady flow on pump rotor vibrations. Similarly, a study by Danilishin et al. (2020) applied FSI to air compressors, highlighting that incorporating flow-induced forces into structural analysis is essential at high pressures to improve the accuracy of structural evaluations.

In addition, the study by Wu et al. (2019) demonstrated how FSI simulation combined with cavitation models can clarify the effect of cavitation bubbles on the forces and pressures acting on pump blades, leading to changes in deformations and natural frequencies, and thereby improving the prediction of fatigue life and structural degradation.

Furthermore, numerous studies have addressed FSI analysis and its applications in investigating vibrations in fans, as well as in estimating service life and fatigue (Badshah et al., 2019; Liu et al., 2023; Santo et al., 2019; Sun et al., 2022).

Despite the growing interest and significant progress in the application of FSI simulations studies, those that address the use of these methods to estimate the fatigue limit and assess the effect of turbulent flow on the service life of industrial centrifugal fans remain extremely scarce. This severe lack of research reduces the accuracy of predicting fan durability under real operating conditions, which may lead to operational issues and high maintenance costs. Therefore, there is an urgent need for dedicated studies to fill this gap and enhance the reliability of centrifugal fan design.

This study aims to fill this research gap by using FSI simulations to evaluate the effect of aerodynamic loads generated by turbulent flow on the service life of the FN280 centrifugal fan. Given the limited availability of detailed geometric data for the fan under investigation and the absence of a ready-made 3D model of its blade, the model was created using reverse engineering techniques, an essential step to ensure the accuracy of the FSI simulation under aerodynamic turbulence conditions.

Accordingly, this study seeks to assess the impact of aerodynamic loads resulting from turbulent flow on the service life of the FN280 centrifugal fan by applying FSI simulation to estimate fluctuating stresses in the fan. The study hypothesizes that these loads significantly contribute to reducing the fan's service life by increasing stress fluctuations.

To achieve this, the aerodynamic loads were calculated using computational fluid dynamics (CFD) simulation, and the structural response was analyzed through transient structural analysis within the framework of FSI simulation, using a one-way coupling approach.

The remainder of this paper is structured as follows: Section 2 describes the fan model and its geometric reconstruction process. Section 3 introduces the adopted fluid–structure interaction (FSI) methodology. Section 4 outlines the numerical modeling approach, including the governing equations, mesh generation, and boundary conditions applied in both CFD and FEA analyses. Section 5 presents and discusses the aerodynamic and structural results. Section 6 summarizes the key findings and conclusions, while Section 7 addresses the study's limitations and suggests directions for future research.

2. DESCRIPTION OF THE FAN UNDER STUDY AND DESIGN

2.1 General Characteristics of the Fan

The centrifugal fan under study is equipped with a single large inlet and is used to transport hot gases containing a limited amount of dust particles, making it suitable for industrial applications, particularly in cement factories. The fan consists of an outer casing, an impeller equipped with a drive shaft, and two bearings. The shaft is made of steel to ensure the strength and durability required to withstand high operational loads and speeds. Spherical thrust roller bearings are used, with the first bearing acting as a guiding element mounted near the motor, while the second bearing is mounted in a way that allows it to move within its housing.

These bearings are installed in cast bearing housings of the FLS type, which are themselves mounted on a metal base to provide the necessary support and stability during operation. To ensure efficient performance under high-temperature conditions, a cooling fan is installed on the shaft near the outer casing (see Fig. 1). The fan impeller consists of 16 backward-curved blades and operates at a rotational speed of 985 revolutions per minute (RPM). The detailed technical specifications of the fan are summarized in Table 1, based on data obtained from the manufacturer's technical datasheet for the FN280.

Table 1 Fan technical data

Type		FN 280
Number of blades		16
Blade thickness		8 [mm]
Impeller tip speed, U2		115.46 [m/s]
Q_d (design flow rate)		53.9 [m3/s]
ΔHd (design Total pressure rise)		6148 (Pa)
Temperature		84 [°C]
Rotational speed,		985 RPM
Roller bearings	bearing 1	22328/C3
	bearing 2	22332/C3

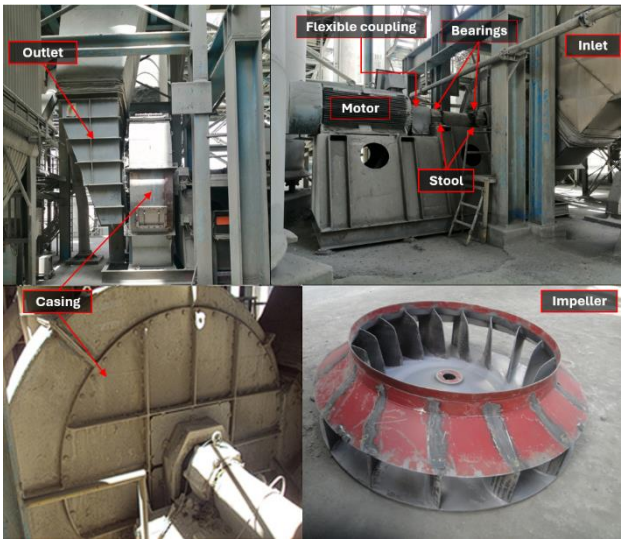

Fig. 1 Pictures of the section where the FN280 centrifugal fan is placed in the plant with pictures of the impeller

Fig. 2 Real photo of a fan blade

2.2. Modeling of the Fan

2.2.1 Reconstruction of the blade using reverse engineering

Due to the unavailability of technical data related to the blade of the FN280 centrifugal fan, shown in Fig. 2, and the complexity of its geometric shape which made it impossible to reconstruct using traditional methods a reverse engineering approach was adopted to recreate its geometry. Reverse engineering is defined as the process of systematically analyzing a physical object to ascertain its specifications and design.

The objective of reverse engineering is to reproduce or modify the object in question. This process goes through several sequential stages, ultimately leading to the creation of a 3D CAD model. Figure 3 presents a schematic

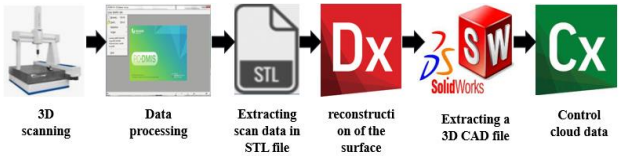

Fig. 3 Reverse engineering stages

illustrating the different stages of the reverse engineering process.

The first stage of the reverse engineering process consists of the scanning phase, during which a Coordinate Measuring Machine (CMM) was used (see Fig. 4a). This device enables high-precision scanning of geometric points on both the outer and lower surfaces of the blade,

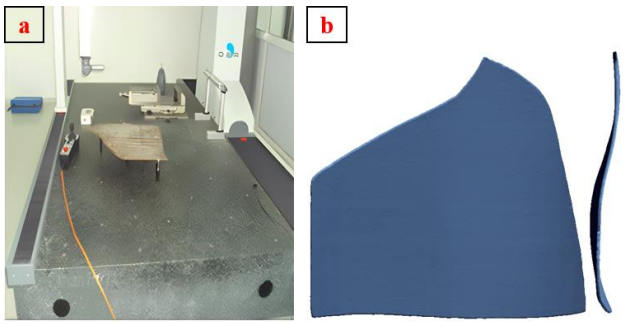

Fig. 4 Blade alignment for Scanning phase a) Blade position on CMM table, b) Digital data of the blade

including the mating surface. Subsequently, the scanned data is converted into a digital representation in the form of a point cloud of the blade, using the PC-DMIS software dedicated to the CMM, with a recorded standard deviation of 0.1 microns. This data is then processed using the tools available in GEOMAGIC DESIGN X (2022). Figure 4.b illustrates the point cloud of the blade.

Given that the collected data contained distortions caused by deviations in the leading and trailing edges, which reflect surface irregularities on the blade, a hybrid modelling technique combining parametric modelling and surface reconstruction was adopted.

This methodology consists of several sub-steps (3D Systems, 2013) (see Fig. 5), with surface reconstruction selected for its effectiveness in handling complex geometric surface shapes. To implement this technique, the mesh regions were first accurately defined using the identification of surfaces. Then, the blade surfaces were manually created using the Mesh fit tool, following the steps in Fig. 6. After generating all surface and reference planes (see Fig. 5.e), the final 3D model of the fan blade was obtained (Fig. 5.f).

2.2.2 Accuracy analysis of the reconstructed blade

The accuracy of the 3D model of the blade was analyzed and evaluated by comparing the CAD model, created using GEOMAGIC DESIGN X (2022) software, with the digital data (point cloud) recorded by the CMM scanning device. Similar approaches employing GEOMAGIC DESIGN X for reverse engineering and geometric reconstruction have been reported in previous studies, confirming its reliability and precision for complex surface modeling (Mahboubkhah et al., 2018; Wu et al., 2022).

This process is carried out using GEOMAGIC CONTROL X (2022) software, where the CAD file of the blade and the STL file containing the scan data must first be imported, as shown in Fig. 6.a and b. After importing, an alignment operation between the CAD and STL files is performed using dedicated tools within the software, as illustrated in Fig. 6.c,

Based on the analysis report generated by the software (Fig. 7), the geometric deviation between the reconstructed model and the scan data was quantified. Figure 7.b presents the statistical distribution of these deviations: the maximum and minimum deviations were +0.0785 mm and −0.0785 mm, respectively, with an

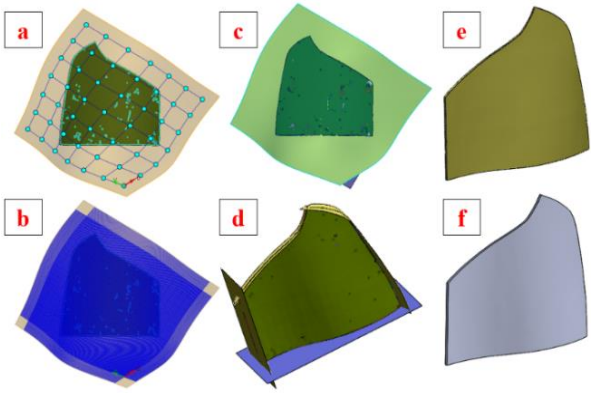

Fig. 5 Fitting Surface Modeling(a) Fitting Region, (b) ISO lines, (c) surface fitting of suction and pressure side, (d) surface-cut, (e) The blade surfaces, (f) Final CAD model of the blade

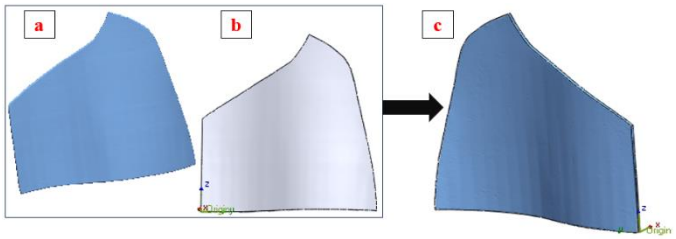

Fig. 6 CAD-ready data file (a) Digital data of the blade, (b) CAD model of the blade, (c) Alignment between CAD and STL

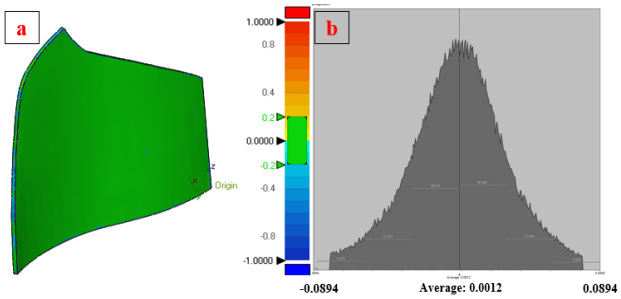

Fig. 7 Verification of the Final Model Accuracy (a) comparison deviation chromatograms, (b) Total distributions of comparison errors

average deviation of just 0.0012 mm. Given the functional and aerodynamic requirements of the blade, these deviations are considered minimal and within acceptable engineering tolerances

Figure 7a displays a color map that visualizes the deviation magnitudes across the blade surfaces. The tolerance range was set between −0.2 mm and +0.2 mm. Regions within this range are shown in green, indicating good agreement between the CAD and scan data. Areas in red and blue indicate surfaces that are slightly oversized or undersized, respectively.

Such small geometric deviations are not expected to significantly affect global stress or fatigue life predictions. However, minor local variations may occur in regions with high stress gradients, such as the blade root and transition fillets. Moreover, it is important to note that the blade root area is subject to welding during

manufacturing, which inherently limits the achievable geometric accuracy in this region. Consequently, slightly larger deviations are considered acceptable at the blade root, without compromising the overall structural or fatigue performance of the component.

2.3. Modeling of the Remaining Components

A precise 3D model of the fan components was created using the engineering modeling techniques provided by SolidWorks. This design included the components for which complete and accurate engineering information was available. The dimensions of these parts were based on direct measurements and original technical drawings. The final assembly of these components was carried out within the SolidWorks environment. Figure 8 illustrates the complete 3D model of the fan.

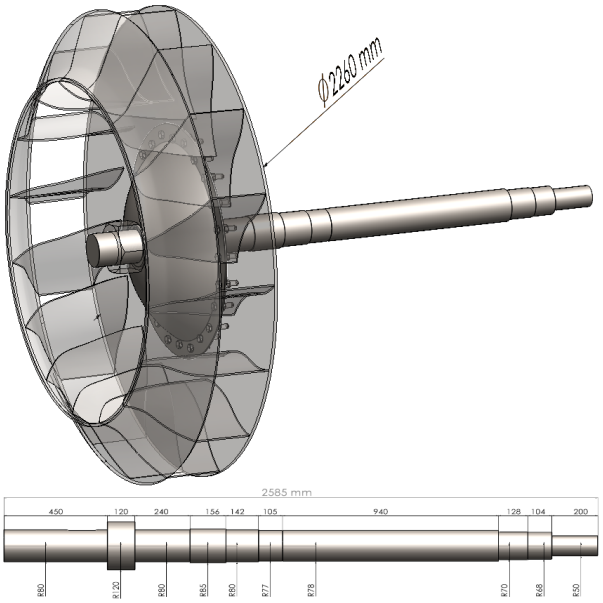

Fig. 8 3D model of FN280 centrifugal fan

3. FLUID-SOLID INTERACTION METHODS

FSI simulation is a branch of multiphysics in which fluid dynamics and structural mechanics are the coupled systems under consideration. The coupling process is represented by the interaction between circumferential or internal fluid flow and moving or deformable structures (Ahamed et al., 2017; Hou et al., 2012). In such problems, both physical fields, their governing equations, and the associated boundary conditions must be satisfied simultaneously. The coexistence of fluid and structural domains inherently produces interaction surfaces, across which information such as forces and displacements is exchanged.

Numerical methods used to solve FSI problems can generally be classified into two main approaches: monolithic methods and partitioned methods. In monolithic methods, the fluid and solid governing equations are solved simultaneously using a single algorithm (a unified matrix formulation). In contrast, partitioned methods solve the equations of each physical field separately and in a sequential manner, with coupling achieved through iterative data exchange between the solvers. In this project, the partitioned approach was adopted, which can be further classified into one-way coupling and two-way coupling.

In the one-way coupling FSI simulation employed in this study, the fluid field is solved independently without considering structural deformation. In this approach, the CFD analysis is carried out until convergence is achieved. The resulting pressure loads are then transferred from the fluid dynamics analysis to the structural analysis (Hou et al., 2012). The schematic representation of the one-way coupling procedure is in Fig. 9.

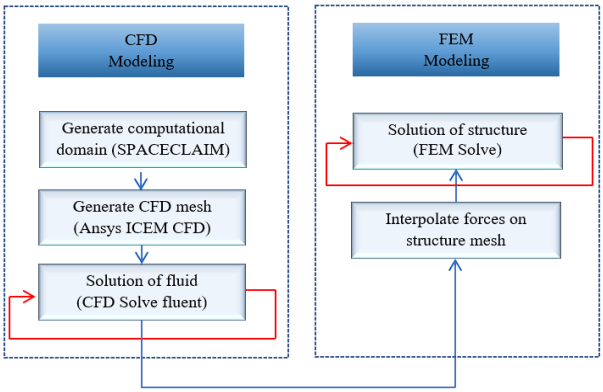

Fig. 9 Schematic diagram of the one-way coupling

In the two-way coupling simulation, the pressure loads obtained from the fluid dynamics analysis are transferred to the structural analysis. In turn, the structural deformations are fed back to the fluid domain, updating the flow solution accordingly. This iterative exchange continues until convergence is achieved and generally requires significantly more computational resources than the one-way coupling method.

4. NUMERICAL MODELLING

4.1 Mathematical Model Formulation

The coupled FSI problem is formulated by combining the governing equations of the fluid and solid domains for the incompressible fluid and the deformable solid, together with appropriate interface coupling conditions (Tu et al., 2015). Let $\Omega_f(t)$ denote the fluid domain, $\Omega_s(t)$the solid domain, and $\Gamma_{fs}(t) = \partial\Omega_f(t) \cap \partial\Omega_s(t)$ the moving interface between them. The outward unit normal are n_f (pointing into the fluid) and $n_s = -n_f$ (pointing into the solid). The primary variables are: fluid velocity v, fluid pressure p, solid displacement u, solid velocity $\dot{u}$, Cauchy stress tensor σ, density ρ, and body force per unit mass f.

The fluid within the fan domain is modeled as an incompressible Newtonian medium with constant density ρ_f and dynamic viscosity μ_f. In Eulerian coordinates, the governing equations are the incompressible Navier-Stokes equation (Ferziger et al., 2019).

$$\nabla . v = 0 \tag{1}$$

$$\rho_f\left(\frac{\partial v}{\partial t}+v.\nabla v\right)=-\nabla p+\mu_f\nabla^2+\rho_f f \tag{2}$$

The Reynolds stresses were modeled using the eddy-viscosity turbulence model namely the SST *k-ω*. The adoption of this model was justified by the high curvature of the impeller blades and its reliable performance in predicting flow separation under adverse pressure-gradient conditions.

In the solid domain, the structure is modeled in a Lagrangian reference frame, where material points are tracked over time. The linear momentum balance is written as:

$$\nabla\cdot\sigma_s+\rho_s f=\rho_s\ddot{u}\ \text{ in }\ \Omega_s(t) \tag{3}$$

with ρ_s the solid density and σ_s the Cauchy stress tensor. The analysis assumes small strains and linear elastic material behavior, the kinematic and constitutive relations are:

$$\varepsilon=\frac{1}{2}\left(\nabla u+(\nabla u)^T\right) \tag{4}$$

$$\sigma_s=\lambda tr(\varepsilon)I+2\mu\varepsilon \tag{5}$$

where ε is the strain tensor, λ and μ are the Lamé constants, given in terms of the Young's modulus $E$and Poisson's ration v by:

$$\lambda=\frac{Ev}{(1+v)(1-2v)} \tag{6}$$

$$\mu=\frac{E}{2(1+v)} \tag{7}$$

At the FSI, displacement compatibility and force equilibrium are enforced to ensure accurate coupling between the two domains on $\Gamma_{fs}(t)$ via kinematic and dynamic continuity:

$$v=\dot{u} \tag{8}$$

No-slip / no-penetration condition

$$\sigma_f n_f=\sigma_s n_s \tag{9}$$

Traction equilibrium

where σ_f is the fluid stress tensor, which for a Newtonian fluid is:

$$\sigma_f=-pI+2\mu_f S \tag{10}$$

With $S=\frac{1}{2}\left(\nabla v+(\nabla v)^T\right)$ the rate-of-strain tensor

4.2 Computational Fluid Dynamics (CFD)

4.2.1 Computational domain of the fan

Due to the use of the one-way coupling FSI method in this study, the fluid field must be solved independently until convergence is reached. Therefore, a computational domain was created, including the inlet and outlet pipes as well as the impeller. The fluid field and flow components were modeled using SPACECLAIM software. A straight section was added at the top of the inlet. To minimize interference from the physical model in the numerical calculations and allow for adequate flow development, the inlet length was extended to twice its diameter. Similarly, to prevent backflow, the outlet was extended to four times its diameter. The CFD analysis of the developed domain was then performed using ANSYS Fluent. Figure 10 illustrates the complete computational domain of the fan.

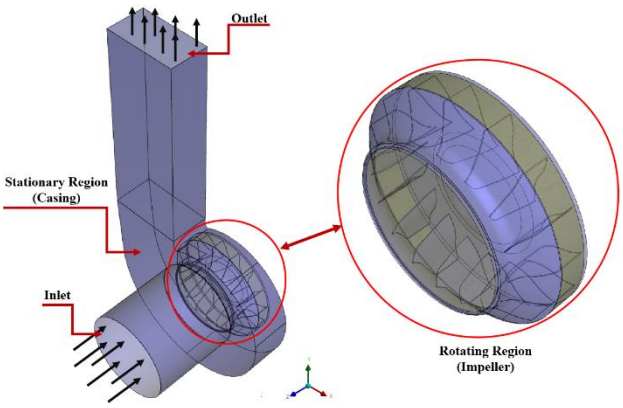

Fig. 10 Computational domain for the fan

4.2.2 Meshing procedure

The mesh of the fluid domain was generated using the ICEM CFD software. To enable the rotation of the fan, the computational domain was divided into separate regions. Due to complexity of the geometry and the large curvature of the impeller blades, an unstructured tetrahedral mesh was applied in areas with complex shapes, rather than throughout the entire domain. Particular attention was given to regions of high importance in the numerical simulation, such as the blade surfaces, the casing neck, and the blade passages inside the impeller. The mesh density was refined in these areas, with a smooth transition from coarse to fine elements. To allow proper flow transfer between rotating and stationary regions, interface boundaries with a non-conformal mesh were used. Figure 11 shows the complete computational domain mesh.

Fig. 11 View of the entire computational domain mesh

Prism layer elements were generated around the blade surfaces to satisfy the mesh accuracy requirements of the several trial simulation to ensure that the non-dimensional wall distance (Y^+)remained within the recommended rang for the SST *k-ω* turbulence model, i.e., $Y^+\leq 1$ (Zigh & Solis, 2013). A total of 12 prism layers were applied along each boundary layer wall (Goetten et al., 2019; van Druenen & Blocken, 2024). Figure 12 presents a cross-section of the impeller mesh, highlighting the near-wall region of the blade surface used in the numerical simulation. The Y^+ values on both the high-

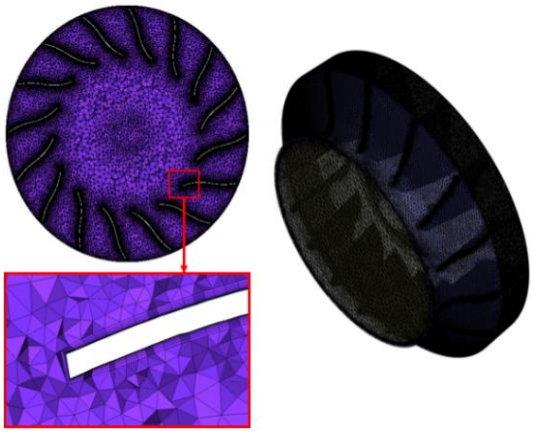

Fig. 12 cross-section of the impeller mesh and the exact mesh in the area near the wall for the blade surface

pressure and low-pressure sides of the blade were meticulously monitored throughout the duration of the simulation process.

To ensure mesh accuracy, the required number of cells was determined using shaft power (W_{shaft}) as an indicator for grid independence. This analysis was conducted under steady-state conditions, with a fixed blade position and at the designed flow rate (Q_d). The numerical results for different mesh sizes are presented in Table 2. As shown, when the number of cells exceeds 5.57 million, further grid refinement has no significant effect on the results. Therefore, a mesh containing 5.57 million cells was selected to reduce computational cost while maintaining accuracy.

4.2.3 Boundary condition

The boundary conditions in this simulation were applied by fixing the volumetric flow rate through prescribing a velocity profile at the inlet and static pressure at the outlet. The velocity profile was adjusted for each flow case under study, and this approach was adopted due to its fast convergence. At the inlet, a uniform velocity profile was imposed for each rate, where four flow cases were considered: $0.89Q_d\left(48\frac{m^3}{s}\right)$, Design flow rate (Q_d), $58.82m^3/s$, and $1.33Q_d\left(72\frac{m^3}{s}\right)$.

At the outlet, atmospheric pressure was imposed as the boundary conduction. To specify the turbulence parameters at the boundaries, uniform values were adapted to represent a medium turbulence level, with turbulence intensity of 5% and turbulence viscosity rate of 10. A no-slip condition was enforced on all wall surfaces.

The SIMPLEC algorithm was employed for pressure–velocity coupling to enhance convergence efficiency in simulations involving a large number of computational cells. Second-order upwind schemes were used for the discretization of convection terms, while central differencing was applied to diffusion terms. For the unsteady simulations, a second-order implicit scheme was utilized to discretize the time-dependent terms.

To maintain numerical stability and provide sufficient temporal resolution for unsteady interactions, a small-time step of 8.46024×10^{-5} was selected. This time step size corresponds to an impeller rotation of 0.5°.

4.2.4 Grid Independence study

To ensure mesh accuracy, the required number of cells was determined using shaft power (W_{shaft}) as an indicator for grid independence. This analysis was conducted under steady-state conditions, with a fixed blade position and at the designed flow rate (Q_d). The numerical results for different mesh sizes are presented in Table 2. As shown, when the number of cells exceeds 5.57 million, further grid refinement has no significant effect on the results. Therefore, a mesh containing 5.57 million cells was selected to reduce computational cost while maintaining accuracy.

Table 2 Sensitivity of grid density on power shaft

number of nodes (Million)	4.3	5.1	5.57	5.58	5.98
W_{shaft} [kw]	495.3	492.1	488.4	488.1	487.9

4.3 Structural Calculation

4.3.1 FEA meshing

For the solid domain, an unstructured tetrahedral mesh was generated to account for the structural load acting on the centrifugal fan, which arises from the pressure distribution obtained in the fluid dynamics analysis. Due to the fan's complex geometry, the SOLID185 element was employed. This element is a 3D solid element with eight degrees of freedom per node, allowing accurate representation of the structural behavior (Aimeur & Menasri, 2022). The mesh consisted of 1,371,960 nodes and 642,749 elements, as illustrated in Fig. 13. The minimum element size was 5 mm, while the maximum element size reached 20 mm.

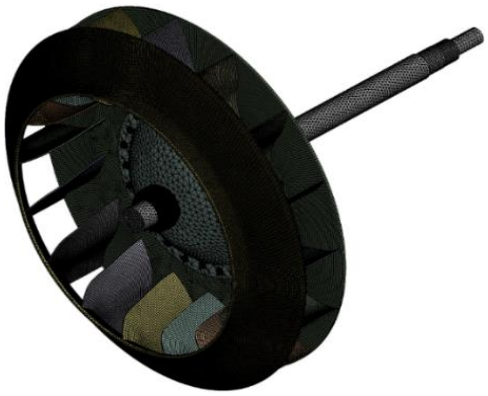

Fig. 13 Meshes for structure

4.3.2 Material properties and assumptions

The impeller, shaft, and supporting structure were made of structural steel. The material properties used in the simulation were as follows: density $\rho = 7850Kg/m^3$, Young's modulus $E = 2.1 \times 10^5 MPa$, and Poisson's ratio $\nu = 0.3$. The material was assumed to behave linearly

elastically under small strain conditions. The contacts between the hub, blades, and shaft were modeled as bonded, assuming perfect adhesion and no relative motion. Geometric simplifications were applied by omitting the screw threads of the bolts and nuts to reduce mesh complexity while preserving the overall stiffness and mass distribution of the model. These assumptions and simplifications allowed achieving a good balance between computational efficiency and result accuracy.

4.3.3 Boundary condition FEA

In the transient structural analysis, performed using ANSYS Mechanical, constraints and loads were applied to the rotor shaft of the centrifugal fan. The loading conditions included the internal and external fluid pressure acting on the fan, as well as the centrifugal force generated by its rotation. The fan operated at a rotational speed 985 RPM, with the centrifugal force applied in the direction of rotation. The flow-field pressure distribution was obtained from the CFD results and transferred to the fan structure through the FSI coupling. The bearing supports of the rotor shaft were simplified to cylindrical representations, which were applied as axial and radial constraints. A fixed time step of 0.001 s was used in the transient structural analysis to ensure numerical stability and convergence.

Figure 14 illustrates the boundary conditions used in the transient structural analysis.

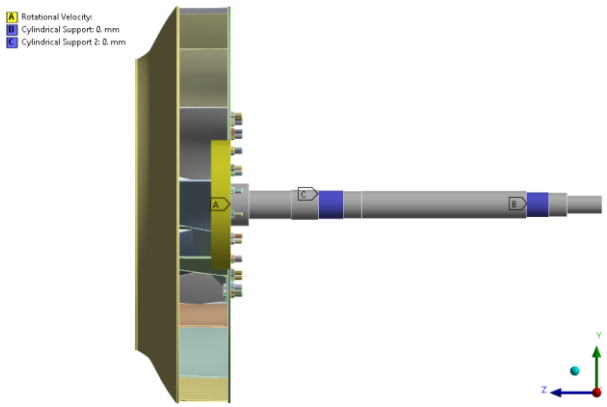

Fig. 14 Boundary conditions applied to the fan

5. RESULTS AND DISCUSSION

5.1 CFD

To validate the modeling approach adopted in this study, the numerical predictions were compared with the experimental data of the FN280 fan. Fig. 15 illustrates the unsteady simulation results, obtained by averaging the computed quantities over the final cycle and comparing them with the corresponding experimental performance curves. The aerodynamic performance of the studied fan was experimentally determined in accordance with the requirements of the industrial fan testing standard ISO 5801. The unsteady solution started to exhibit periodic behavior after approximately 1.5 impeller rotations. Each time step was iterated until the residuals were reduced to 10^{-6} for the continuity equation and 10^{-5} for the momentum and turbulence quantities. On average, 15 iterations per time step were sufficient to achieve the specified convergence criteria. Each operating point required approximately 15 days of computation on a 12-core CPU with 128 GB of RAM, owing to the fine time-step resolution and high mesh density adopted in this study.

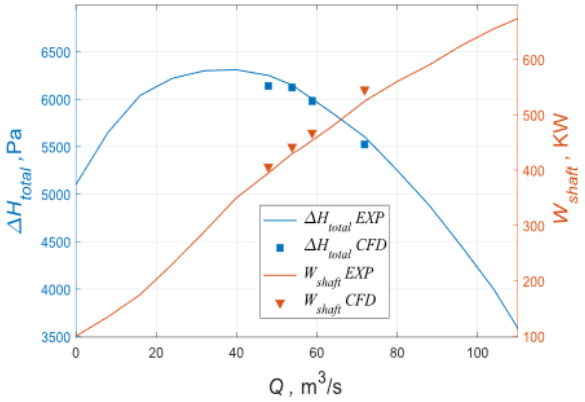

Fig. 15 Numerical results validation $(\Delta H_{total} - Q, W_{shaft} - Q)$

The results in Fig. 15 show that the unsteady simulation curve closely follows the experimental performance curve, with only minor deviations, thereby confirming the reliability of the approach in predicting the fan's flow field. The time-averaged total pressure rise was underestimated by up to 2.55% at a flow rate of 0.89 Q_d, and by 0.39% at the design operating flow rate. Conversely, the shaft power was overestimated by up to 3.81% at the flow rate of 1.33Q_d.

Overall, Fig. 15 indicates that the shaft-power deviation correlates with the flow rate. These discrepancies fall within the typical range reported in the literature for centrifugal fans and compressors, where deviations between CFD and experimental data usually range from 2% to 6% and may increase up to 9% under off-design conditions (Ivanov et al., 2022; Nagaraj & Karanth, 2023). Hence, the present model demonstrates a satisfactory predictive capability and can be considered reliable for further analysis of the fan's internal flow field.

To better understand the flow and structural behavior of the centrifugal fan, three cross sections, Z1, Z2, and Z3, were created on the rotation axis at different areas of the impeller, where Z1 = 0.04 m, Z2 = 0.14 m, and Z3 = 0.24 m, as shown in Fig. 16, the static pressure and flow velocity are shown in different areas of the impeller and the casing area. These are shown according to the design flow rate.

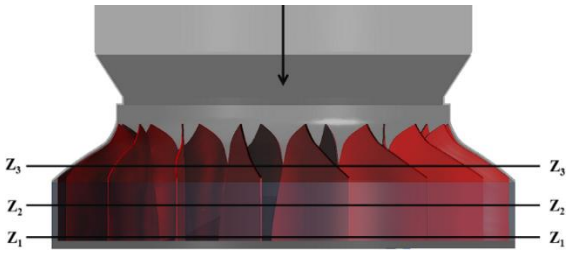

Fig. 16 Cross sections Z1, Z2, and Z3

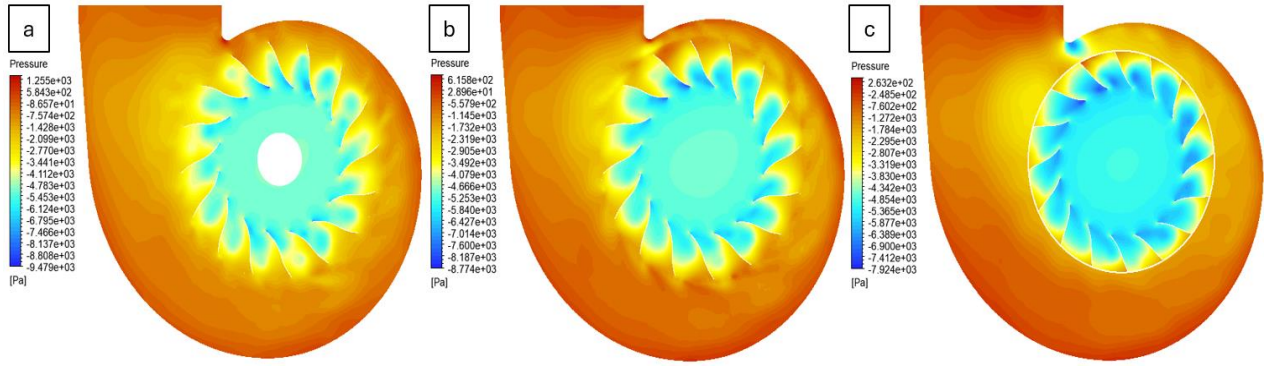

Fig. 17 Pressure contours on cross-section at design flow rate Q_d a) Z1, b) Z2, c) Z3

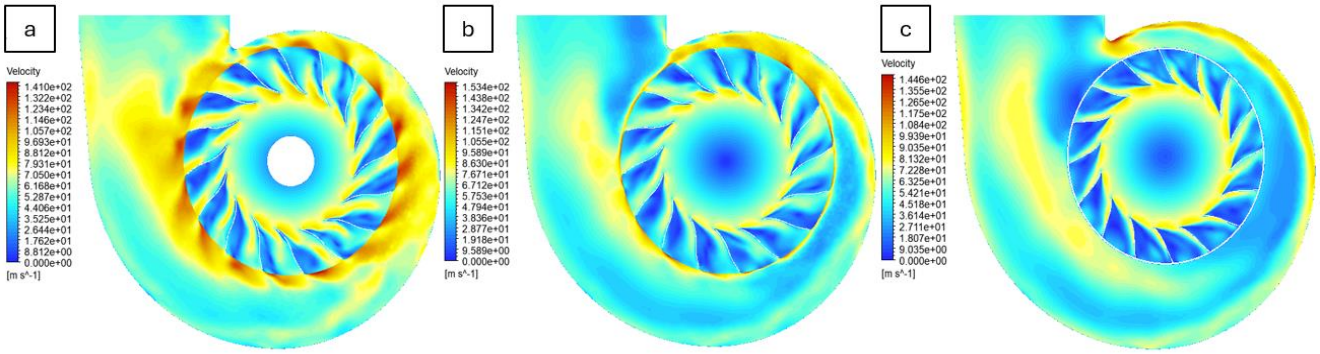

Fig. 18 Velocity contours on cross-section at design flow rate Q_d a) Z1, b) Z2, c) Z3

Figure 17 show the distribution of pressure at the level of the cross sections Z1, Z2, and Z3, respectively. The figure depicts that the pressure has almost the same distribution in Z1 and Z2, and the difference is in the maximum and minimum values, as it appears from the figure that the pressure increases as the impeller enters the outlet, and the pressure value is at its maximum at the neck of the casing.

When the impeller rotates, this results in the conversion of dynamic pressure into static pressure along the length of the housing, with a high-pressure gradient in the radial direction. As for the distribution of pressure on the cross-section Z3, it is slightly different, especially at the tip of the housing flap, where it is at the lowest value due to its location, which is at the top of the impeller blade, and the pressure is lower than that when compared to Z1 and Z2.

As for the blade passages (from blade to blade) of the impeller, the pressure on the suction side is lower than on the pressure side of the blade, as at the tip of the front edge of the blade, the pressure is at its lowest value. It can also be noted that when the blade passes in front of the cover tongue, the pressure is higher, and when the blade rotates from the neck of the casing to the large discharge section of the helix, the pressure decreases. This is due to the asymmetric helix geometric design, which in turn leads to the pressure being distributed on the blades in an irregular state.

Our observations regarding the similarity in pressure patterns between Z1 and Z2 are consistent with previous studies on centrifugal fans operating at low flow rates. In one such study, it was reported that the first section (Z=0.015 m) and the second section (Z=0.030 m) exhibited nearly identical pressure profiles despite their different axial positions, whereas the upper section displayed a more uniform distribution (Lun et al., 2019).

Additional investigations have confirmed that both velocity and static pressure increase with the rotor radius, which is consistent with the pressure rise toward the outlet tip observed in our results (Lun et al., 2019). Similarly, an analysis on the internal flow in a three-stage rotor demonstrated that the increase in total pressure can induce vortices and backflow inside the passages, explaining the non-uniform distribution observed in Z3 (Ding et al., 2019).

Figure 18 illustrate the velocity distribution across the three cross-sections Z1, Z2, and Z3, respectively, under the design flow condition. The results reveal noticeable variations in both the distribution and magnitude of the flow velocity among the three sections. Specifically, the lowest velocity values are observed in the tongue region at Z1 and Z2, whereas in Z3 the same area exhibits relatively higher velocity values. The behavior is mainly attributed to the large curvature of the blades, which strongly influences the local flow acceleration.

High-velocity regions are also identified at the loading edges of the blades, near the pressure side, and at the impeller outlet. The velocity contours also show that there are flow interruptions in most of the blade passages right after the leading edge. This shows how important the blade inlet angle is in controlling the flow entering the impeller channels. The tongue region is characterized as a stagnation zone where flow separation is consistently present across all three sections. This phenomenon is primarily caused by the inappropriate blade inlet angle

combined with excessive blade curvature, which prevents the incoming flow from being properly guided around the impeller passages.

In summary, the findings suggest that optimizing the blade inlet angle and reducing the excessive blade curvature are essential design considerations, as they can minimize flow separation and enhance the overall aerodynamic performance of the impeller.

Our observations regarding the low flow velocity near the tongue region in Z1 and Z2 and its subsequent increases in Z3 are consistent with previous research emphasizing the role of blade inlet angle and curvature reduction in enhancing fan performance. Several studies have reported that the velocity profile within blade passages is strongly affected by inlet and outlet geometry and that optimizing these angles helps reduce flow disturbances and improve overall flow uniformity (Wang et al., 2022). Furthermore, Ren et al. (2019) demonstrated that decreasing the blade angle and refining its distribution can effectively mitigate flow separation and significantly enhance the hydraulic efficiency of pumps, which is consistent with the results obtained in this study.

5.2 Results Finites Elements Method

The one-way coupled FSI simulation provides valuable insights into how various components of a centrifugal fan structurally respond to aerodynamic loads obtained from transient CFD analysis. The aerodynamic pressure field is mapped onto the structural model to conduct transient structural analysis. The results include the displacement and stress distributions, along with a fatigue limit estimate. This estimate helps assess whether the transient fluid pressure should be considered in fatigue life predictions

Figures 19 and 20 illustrate the total deformation behavior of the rotor under flow-induced loads as obtained from a one-way FSI simulation. Fig. 19 shows that the maximum deflection (≈ 5.0 mm) occurs at the leading edge of the impeller blades. Similar findings have been reported in numerical studies of pumps and turbomachinery, where deformation decreases from the blade tip to the root, with the highest values consistently located at the leading edge or the outer periphery of the rotor (Pei et al., 2016).

Figure 20 further indicates that the transient oscillations of deformation gradually decay over time, reflecting the stabilization of the rotating system. A rough engineering estimate based on the CFD pressure field confirms the plausibility of this displacement magnitude. However, as highlighted by recent studies on rotating blades (Algolfat et al., 2022), the effect of centrifugal stiffening can significantly reduce the net deformation (by up to ~21.5% along the shaft direction). Therefore, the reported maximum value should be interpreted with caution and ideally validated through a steady-state structural analysis or a two-way FSI model, as well as by performing mesh convergence and refined contact modeling to avoid numerical stress spikes.

Figures 21 and 22 depict the equivalent von Mises

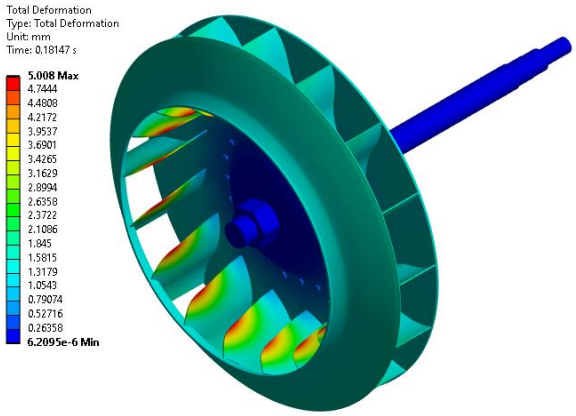

Fig. 19 Contour of the total deformation of the rotor

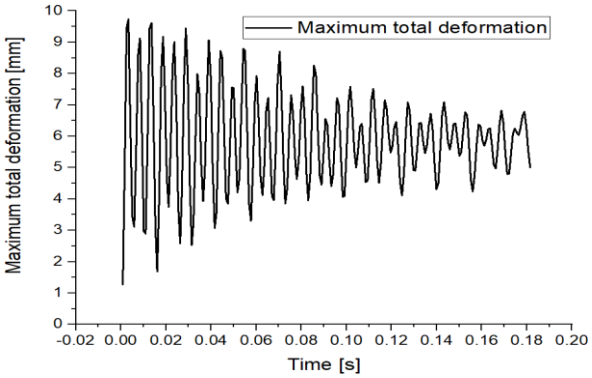

Fig. 20 Time history of maximum total deformation

stress distribution and its time history on the rotor under one-way FSI loading. Figure 21 shows that the maximum stress (~867 MPa) is concentrated at the blade-disk junction—consistent with findings in centrifugal pump/impeller FEA studies, which often report stress concentrations at the blade root or hub interface where bending and aerodynamic loads combine (Bai et al., 2022).

Figure 22 reveals that the stress oscillates cyclically, with transient peaks sometimes exceeding 1.8 GPa. These peaks are likely numerical artifacts (stress spikes) induced by the bonded contact assumption and mesh-related discontinuities—an effect highlighted in several FSI studies (Bang et al., 2022; Wang et al., 2014; Wong et al., 2013). A mesh refinement analysis confirmed that the stress distribution in the critical regions stabilized with finer mesh densities, indicating numerical convergence. These localized spikes have a negligible influence on the global fatigue life estimation, as the fatigue analysis relies on the averaged cyclic stress amplitude rather than isolated peak values. Nevertheless, future work will consider smoother contact modeling (e.g., merged mesh or frictional contact) and two-way FSI simulations to further enhance prediction accuracy.

Fatigue is considered a weakening of the material that results from repeated application of loads, and it can also be considered crack growth since when a load is applied each time, the cracks grow slightly. Average stress and alternating stress are parameters that have a significant

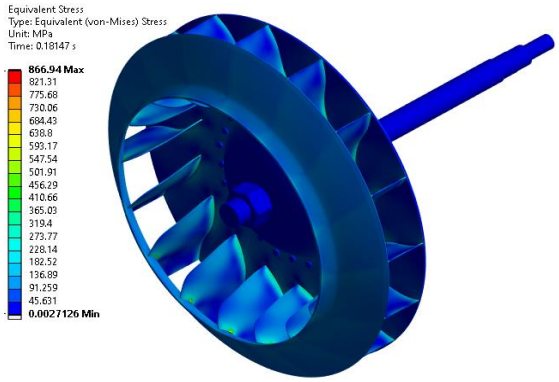

Fig. 21 Contour of the equivalent von Mises stress of the rotor

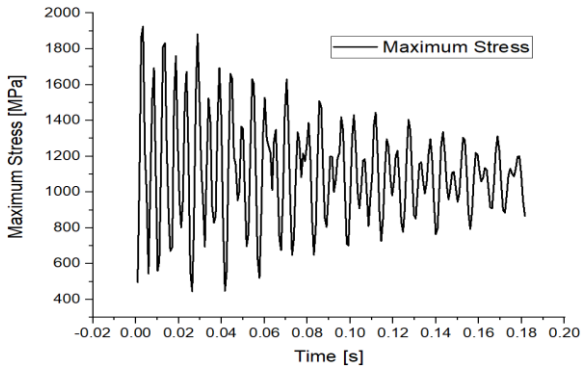

Fig. 22 Time history of maximum equivalent von Mises stress

impact on the fatigue life of the fan, as fatigue strength increases with a decrease in alternating stress and/or average stress, and fatigue strength decreases with an increase in one or both of them. To verify the fatigue behavior for the current study, a lifetime fatigue model was used to conduct fatigue analysis. The model does not differentiate between crack initiation and propagation, and the fatigue life determines the total life of the joint and is based on the S-N curve of the material, which is often established from experimental tests. The fatigue life model also deals with high cycle stress, and the stress ratio $\left(R=\sigma_{\min}/\sigma_{\max}\right)$ is used.

The fatigue and stress model for the fatigue unit allows the inclusion of average stress effects through direct interpolation between the experimental S-N data. Due to the unavailability of this experimental data, experimental relationships can be used that work to use the experimental relationships for the properties of static materials with the S-N data, which enables us to calculate the average stress effects. The Gerber equation was used because the fan used in the current study is made of iron. It was also used in the fatigue analysis as a stress element to convert the multi-axial stress obtained from the FEA to the uniaxial stress state for the experimental fatigue data, which is the equivalent stress (von-mises).

The fan is manufactured from iron material whose mechanical behavior is comparable to standard structural steel. Therefore, the "Steel Standard" dataset from the ANSYS material library was employed for fatigue and S-N analysis, providing consistent and validated reference data in the absence of specific experimental material

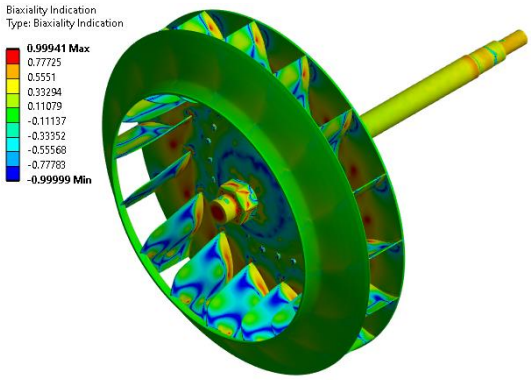

Fig. 23 Biaxiality indication for the rotor

properties. This approach ensures that the overall fatigue trends and critical regions remain accurately represented, even if minor deviations in material parameters exist.

The results of the biaxiality indication analysis revealed that most regions of the rotor are subjected to uniaxial stress (Fig. 23), as indicated by the dominant green color across the majority of the blades. This corresponds to biaxiality values ranging between 0.1 and 0.33, confirming that the structural behavior of most of the rotor body can be accurately represented using an equivalent uniaxial stress state. In contrast, localized regions exhibited biaxial stress (highlighted in red, 0.78–0.99) or pure shear (highlighted in blue, −0.33 to −0.77), predominantly concentrated at the blade roots and geometric transitions. These areas correspond to zones of increased sensitivity to fatigue initiation, consistent with the observed damage patterns.

The color legend indicates the type of stress according to the biaxiality parameter, where +1 corresponds to pure biaxial tension, 0 to uniaxial tension, and −1 to pure shear (see Table 3).

Table 3 Biaxiality values and corresponding stress types in different regions

Region	Stress Type	Biaxiality Value
Blade root	Biaxial	0.78 – 0.99
Mid blade	Uniaxial	0.10 – 0.33
Tip / Transition areas	Pure shear	−0.33 – −0.77

The fatigue safety factor distribution (Fig. 24) reveals that most of the rotor regions exhibit values between 1 and 5, corresponding to moderate stress levels caused by combined centrifugal and bending effects. The highest safety factor, reaching approximately 15, is observed in the hub and support zones, where the stress amplitude remains minimal due to their proximity to the rotational axis and limited deformation. This spatial variation reflects the realistic mechanical behavior of the fan, in which the outer blade sections sustain higher dynamic loads, while the central regions remain largely safe throughout operation.

This trend is consistent with previous investigations on centrifugal fans, which also reported higher fatigue sensitivity near the blade root and lower stress concentration in the hub region (He et al., 2021; Nan et al., 2024a; Ul-Hamid et al., 2015).

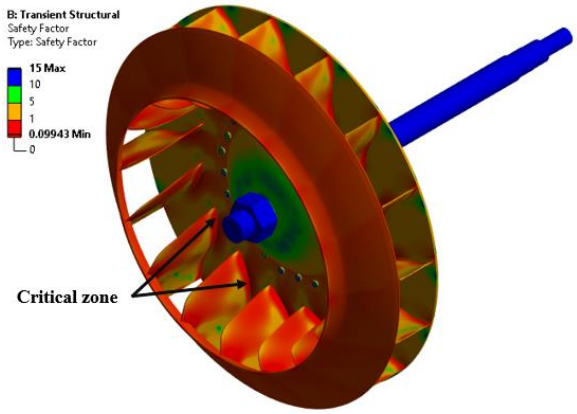

Fig. 24 Fatigue factor of safety for the rotor

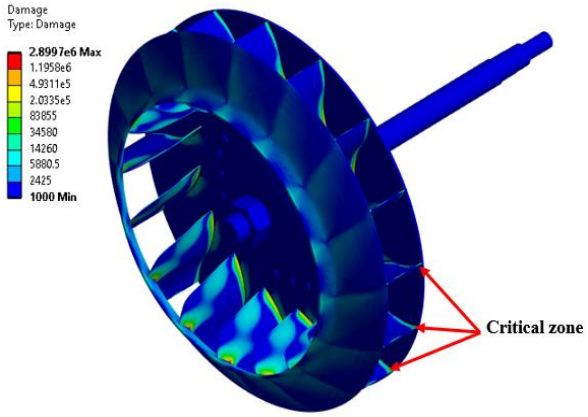

Fig. 25 fatigue damage

Table 4 summarizes the numerical range of the safety factor corresponding to critical and safe regions.

Table 4 Numerical range of the safety factor corresponding to critical and safe regions

Parameter	Value	Location
Maximum safety factor	15	Hub and support (safe region)
Minimum safety factor	0.99 (<1)	Blade root, shaft junction (critical)
Threshold value	1	Critical limit

In Fig. 25, the fatigue damage map revealed that the majority of the fan regions experience negligible damage (values close to the lower range of ~10^3), whereas localized zones at the blade root and shaft junction exhibited markedly higher damage values, reaching approximately 2.89×10^6, which exceeds the reference critical value of 1. This indicates that failure is most likely to initiate in these regions before the rotor attains its overall design life. The color legend has been refined and supplemented with annotations to highlight these critical locations, while a numerical summary shows: Max damage ≈ 2.89×10^6 (critical) and Min damage ≈ 1.0×10^3 (negligible).

In Table 5 annotations highlight the most affected zones, and the corresponding numerical data are summarized below.

Table 5 Damage Levels and Most Affected Zones

Maximum damage	2.89×10^6 (>1)	Failure initiation likely (local zones)
Minimum damage	1.0×10^3	Negligible
General trend	<1 in most regions	Safe operation
Maximum damage	2.89×10^6 (>1)	Failure initiation likely (local zones)

The effect of cyclic stresses on the centrifugal fan was simulated using an approach similar to that adopted by Dadhich et al. (2015) who employed ANSYS in combination with Gerber's theory to calculate fatigue life and safety factors, which is consistent with the methodology applied in this study. The analytical results of this work were also in good agreement with findings based on Miner's cumulative damage method for predicting blade life, as demonstrated in studies on high-speed train cooling system fans (He et al., 2021). Furthermore, this study accounted for the role of geometric design in stress distribution, in line with recent research highlighting the influence of blade thickness and casing configuration on the fatigue life of centrifugal rotors (Radgolchin & Anbarsooz, 2023).

6. CONCLUSION

3D FSI simulations were performed using the ANSYS Workbench platform through a one-way coupling strategy. Aerodynamic loads were computed in ANSYS Fluent and then transferred to the structural module for transient stress and fatigue analysis. The study focused on the FN280 centrifugal fan installed in a cement plant, with the blade geometry reconstructed by reverse engineering to ensure accurate representation.

The aerodynamic field obtained from CFD was validated against experimental performance data. The deviation in total pressure rise at the design flow rate was only 0.39%, while the maximum deviation in shaft power reached 3.81% at off-design conditions. These deviations, all within 4%, confirm the reliability of the aerodynamic loads used in the subsequent structural and fatigue analyses.

Based on these validated aerodynamic loads, the structural analysis showed negligible deformations due to the high stiffness of iron relative to the aerodynamic pressures. The fatigue assessment revealed that the majority of fan regions are safe, with fatigue safety factors up to approximately 15, corresponding to a predicted fatigue life of about 2.8×10^6 cycles. Nevertheless, localized critical zones were identified near the blade root and the shaft junction, where the safety factor dropped below 1, indicating a high probability of premature failure before the overall design life.

Despite these findings, certain limitations must be acknowledged. The analysis was carried out using a one-way FSI approach, which neglects feedback from structural deformation to the flow field. In addition, the material data used in fatigue evaluation were generic, and direct experimental validation of stresses and fatigue life

could not be performed due to the lack of a physical prototype. Furthermore, although the blade was reconstructed via reverse engineering, minor geometric discrepancies may still exist.

Future work will focus on addressing these limitations by:

- Incorporating experimental fatigue data and literature-based benchmarks to strengthen the validation of stress and fatigue predictions;
- Refining the blade geometry and improving the modeling of geometric transitions;
- Adapting the model to simulate off-design and transient operating conditions involving variable rotational speeds, flow rates, and environmental factors through comprehensive parametric studies;
- Adapting the model to simulate off-design and transient operating conditions, including variable rotational speeds, flow rates, and environmental factors, in order to assess their impact on fatigue life predictions through comprehensive parametric studies;
- Upgrading the coupling approach to a fully coupled two-way FSI scheme to better capture the mutual aerodynamic–structural interactions, particularly under highly unsteady conditions.

These planned improvements will enhance the accuracy and reliability of fatigue life predictions and broaden the applicability of the developed framework to industrial centrifugal fans.

CONFLICT OF INTEREST

The authors declare that they have no financial or non-financial conflicts of interest to disclose.

AUTHOR CONTRIBUTIONS

N. Aimrur: Conceptualization, Methodology, Investigation, Data curation, Formal analysis, Writing – original draft. **A. Amour:** Methodology, Formal analysis, Writing, review & editing. **N. Menasri:** Investigation, Data curation, Validation. All authors: Writing review & editing, Approval of the final manuscript.

REFERENCES

Ahamed, M., Atique, S., Munshi, M., & Koiranen, T. (2017). A Concise Description of One Way and Two Way Coupling Methods for Fluid-Structure Interaction Problems. *American Journal of Engineering Research (AJER), 6*, 86–89. www.ajer.org

Aimeur, N., & Menasri, N. (2022). Computational Investigation of Vibration Characteristics Analysis for Industrial Rotor. *Acta Mechanica et Automatica, 16*(4), 373–381. https://doi.org/10.2478/ama-2022-0044

Algolfat, A., Wang, W., & Albarbar, A. (2022). Study of Centrifugal Stiffening on the Free Vibrations and Dynamic Response of Offshore Wind Turbine Blades. *Energies, 15*(17), 6120. https://doi.org/10.3390/en15176120

Alphin, D. S., Zindani, M. N., Mohammed, R. P., & Dhamande, L. S. (2025). Condition Monitoring of Forced-Draft Fan Using Vibration Analysis: A Case Study. *Engineering Proceedings, 93*(1), 9. https://doi.org/10.3390/ENGPROC2025093009

Badshah, M., Badshah, S., Van Zwieten, J., Jan, S., Amir, M., & Malik, S. A. (2019). Coupled fluid-structure interaction modelling of loads variation and fatigue life of a full-scale tidal turbine under the effect of velocity profile. *Energies, 12*(11). https://doi.org/10.3390/en12112217

Bai, M., Tan, H., & Liu, Z. (2022). Numerical study on airflow performance and mechanical characteristics of centrifugal fan. *E3S Web of Conferences, 356*. https://doi.org/10.1051/e3sconf/202235604016

Bang, C. S., Rana, Z. A., Rodriguez, V. M., & Temple, C. (2022). Composite Wing in the Presence of Ground Effect. https://doi.org/10.3390/fluids7020085

Choi, J. S., McLaughlin, D. K., & Thompson, D. E. (2003). Experiments on the unsteady flow field and noise generation in a centrifugal pump impeller. *Journal of Sound and Vibration, 263*(3), 493–514. https://doi.org/10.1016/S0022-460X(02)01061-1

Dadhich, M., Kumar Jain, S., Sharma, V., Kumar Sharma, S., & Agarwal, D. (2015). Fatigue (FEA) and Modal Analysis of a Centrifugal Fan. *International Journal of Recent Advances in Mechanical Engineering, 4*(2), 77–91. https://doi.org/10.14810/ijmech.2015.4209

Danilishin, A., Petrov, A., Kozhukhov, Y., Kartashov, S., Ivanov, V., & Zuev, A. (2020). Fluid - structure interaction analyze for the centrifugal compressor 3d impellers. *IOP Conference Series: Materials Science and Engineering, 1001*(1). https://doi.org/10.1088/1757-899X/1001/1/012010

Ding, W., Chen, Y., & Ding, Y. (2019). Analysis of internal flow field for a three-stage centrifugal fan under various operating conditions. *The Journal of Engineering, 2019*(13), 328–334. https://doi.org/10.1049/joe.2018.9017

Fakhfekh, M., Ben Amira, W., Abid, M., & Maalej, A. (2025). Exploring the influence of flexibility on rotor performance in turbulent flow environments. *European Journal of Mechanics, B/Fluids, 109*, 199–212. https://doi.org/10.1016/j.euromechflu.2024.10.002

Ferziger, J. H., Perić, M., & Street, R. L. (2019). Computational Methods for Fluid Dynamics, Fourth Edition. In *Computational Methods for Fluid Dynamics*. https://doi.org/10.1007/978-3-319-99693-6

Goetten, F., Felix, D., Marino, M., Bil, C., Havermann,

M., & Braun, C. (2019). A review of guidelines and best practices for subsonic aerodynamic simulations using RANS CFD. *11th Asia-Pacific International Symposium of Aerospace Technology, December*, 227–245.

He, N., Feng, P. F., Li, Z. W., Tan, L. G., Pang, T., Chen, Y. Z., & Yang, C. (2021). Fatigue life prediction of centrifugal fan blades in the ventilation cooling system of the high-speed-train. *Engineering Failure Analysis, 124*(December 2020). https://doi.org/10.1016/j.engfailanal.2021.105373

Hou, G., Wang, J., & Layton, A. (2012). Numerical methods for fluid-structure interaction - A review. *Communications in Computational Physics, 12*(2), 337–377. https://doi.org/10.4208/cicp.291210.290411s

Ivanov, V., Kozhukhov, Y., Danilishin, A., Yablokov, A., & Sokolov, M. (2022). Verification and validation of cfd modeling for low-flow-coefficient centrifugal compressor stages. *Energies, 15*(1), 181. https://doi.org/10.3390/en15010181

Li, Q., Zhang, R., & Xu, H. (2023). Effects of Volute Structure on Energy Performance and Rotor Operational Stability of Molten Salt Pumps. *Journal of Applied Fluid Mechanics, 16*(8), 1615–1626. https://doi.org/10.47176/jafm.16.08.1741

Liu, R., Sun, Y., & Ni, J. (2023). Geometric deformation prediction of a centrifugal impeller considering welding distortion and fluid-structure interaction. *Journal of Manufacturing Processes, 96*, 80–98. https://doi.org/10.1016/j.jmapro.2023.04.023

Liu, X., & Liu, J. (2024). Aerodynamic noise characteristics of a centrifugal fan in high-altitude environments. *PLoS ONE, 19*(1 January), 1–18. https://doi.org/10.1371/journal.pone.0296907

Lun, Y., Ye, X., Lin, L., Ying, C., & Wei, Y. (2019). Unsteady characteristics of forward multi-wing centrifugal fan at low flow rate. *Processes, 7*(10), 691. https://doi.org/10.3390/pr7100691

Mahboubkhah, M., Aliakbari, M., & Burvill, C. (2018). An investigation on measurement accuracy of digitizing methods in turbine blade reverse engineering. Proceedings of the Institution of Mechanical Engineers, Part B: *Journal of Engineering Manufacture, 232*(9), 1653–1671. https://doi.org/10.1177/0954405416673681

More, K. C., Dongre, S., & Deshmukh, G. P. (2020). Experimental and numerical analysis of vibrations in impeller of centrifugal blower. *SN Applied Sciences, 2*(1), 1–14. https://doi.org/10.1007/s42452-019-1853-x

Nagaraj, M., & Karanth, K. V. (2023). Numerical Investigations and Artificial Neural Network-Based Performance Prediction of a Centrifugal Fan Having Innovative Hub Geometry Designs. *Applied System Innovation, 6*(6), 104. https://doi.org/10.3390/asi6060104

Nan, G., Yao, X., Yang, S., Yao, J., & Chen, X. (2024a). Vibrational responses and fatigue life of dynamic blades for compressor in gas turbines. *Engineering Failure Analysis, 156*(October 2023), 107827. https://doi.org/10.1016/j.engfailanal.2023.107827

Ottersten, M., Yao, H. D., & Davidson, L. (2022). Inlet gap effect on aerodynamics and tonal noise generation of a voluteless centrifugal fan. *Journal of Sound and Vibration, 540*(May), 117304. https://doi.org/10.1016/j.jsv.2022.117304

Pei, J., Meng, F., Li, Y., Yuan, S., & Chen, J. (2016). Fluid-structure coupling analysis of deformation and stress in impeller of an axial-flow pump with two-way passage. *Advances in Mechanical Engineering, 8*(4), 1–11. https://doi.org/10.1177/1687814016646266

Radgolchin, M., & Anbarsooz, M. (2023). Investigating the effects of shroud and blade thickness profiles on aeromechanical behavior and fatigue-life of 17-4PH impellers. *International Journal of Pressure Vessels and Piping, 204*, 104948. https://doi.org/10.1016/j.ijpvp.2023.104948

Ren, Y., Zhu, Z., Wu, D., Li, X., & Jiang, L. (2019). Investigation of flow separation in a centrifugal pump impeller based on improved delayed detached eddy simulation method. *Advances in Mechanical Engineering, 11*(12), 1–13. https://doi.org/10.1177/1687814019897832

Santo, G., Peeters, M., Van Paepegem, W., & Degroote, J. (2019). Dynamic load and stress analysis of a large horizontal axis wind turbine using full scale fluid-structure interaction simulation. *Renewable Energy, 140*, 212–226. https://doi.org/10.1016/j.renene.2019.03.053

Sun, P., Zhou, L., Wang, Z. X., & Shi, J. W. (2022). Fluid-Structure Interaction Study of the Serpentine Nozzle for Turbofan. *Journal of Applied Fluid Mechanics, 15*(5), 1735–3572. https://doi.org/10.47176/jafm.15.05.1165

3D Systems, I. (2013). Geomagic Design X User Guide. 3D Systems. www.geomagic.com/

Tu, J., Inthavong, K., & Wong, K. K. L. (2015). Computational Fluid Structure Interaction. https://doi.org/10.1007/978-94-017-9594-4_5

Ul-Hamid, A., Al-Hadhrami, L. M., Mohammed, A. I., & Al-Yousef, F. K. (2015). Failure analysis of an impeller blade. *Materials and Corrosion, 66*(3), 286–295. https://doi.org/10.1002/maco.201307362

van Druenen, T., & Blocken, B. (2024). CFD simulations of cyclist aerodynamics: Impact of computational parameters. *Journal of Wind Engineering and Industrial Aerodynamics, 249*(April). https://doi.org/10.1016/j.jweia.2024.105714

Wang, C., Shi, W., Si, Q., & Zhou, L. (2014). Numerical calculation and finite element calculation on impeller of stainless steel multistage centrifugal pump. *Journal of Vibroengineering, 16*(4), 1723–1734.

https://www.extrica.com/article/15031

Wang, D., Zhang, F., Xu, L., Qiu, W., & Zhu, W. (2022). Analysis of the Impact of Inlet and Outlet Installation Angle on CFD Performance of Centrifugal Fan. *Advances in Transdisciplinary Engineering, 30*, 597–602. https://doi.org/10.3233/ATDE221074

Wei, Y., Wang, J., Xu, J., Wang, Z., Luo, J., Yang, H., Zhu, Z., & Zhang, W. (2022). Effects of Inclined Volute Tongue Structure on the Internal Complex Flow and Aerodynamic Performance of the Multi-Blade Centrifugal Fan. *Journal of Applied Fluid Mechanics, 15*(3), 901–916. https://doi.org/10.47176/jafm.15.03.32847

Wolfram, D., & Carolus, T. H. (2010). Experimental and numerical investigation of the unsteady flow field and tone generation in an isolated centrifugal fan impeller. *Journal of Sound and Vibration, 329*(21), 4380–4397. https://doi.org/10.1016/j.jsv.2010.04.034

Wong, K. K. L., Thavornpattanapong, P., Cheung, S. C. P., & Tu, J. (2013). Numerical stability of partitioned approach in fluid-structure interaction for a deformable thin-walled vessel. *Computational and Mathematical Methods in Medicine, 2013*. https://doi.org/10.1155/2013/638519

Wu, D., Ren, Y., Mou, J., Gu, Y., & Jiang, L. (2019). Unsteady Flow and Structural Behaviors of Centrifugal Pump under Cavitation Conditions. *Chinese Journal of Mechanical Engineering (English Edition), 32*(1). https://doi.org/10.1186/s10033-019-0328-8

Wu, Z., Wang, Y., Mo, Y., Zhu, Q., Xie, H., Wu, H., Feng, M., & Mian, A. (2022). Multiview Point Cloud Registration Based on Minimum Potential Energy for Free-Form Blade Measurement. IEEE *Transactions on Instrumentation and Measurement, 71*. https://doi.org/10.1109/TIM.2022.3169559

Zhang, H., You, H., Lu, H., Li, K., Zhang, Z., & Jiang, L. (2020). CFD-Rotordynamics Sequential Coupling Simulation Approach for the Flow-Induced Vibration of Rotor System in Centrifugal Pump Hehui. *Applied Sciences (Switzerland), 10*(3). https://doi.org/10.3390/app10031186

Zhou, J., Jin, G., Ye, T., & Wang, X. (2023). Fluid-induced vibration analysis of centrifugal pump including rotor system based on Computational Fluid Dynamics and Computational Structural Dynamics coupling approach. *Ocean Engineering, 288*, 115993. https://doi.org/10.1016/j.oceaneng.2023.115993

Zhou, L., Liang, K., Zheng, D., Wang, C., Li, M., He, T., Guo, L., & Zheng, L. (2025). Vibration Characteristics Analysis and Structural Optimization of a Volute-Less Centrifugal Fan Frame. *Applied Sciences (Switzerland), 15*(9). https://doi.org/10.3390/app15095069

Zigh, G., & Solis, J. (2013). Computational fluid dynamics best practice guidelines for dry cask applications: Final report (NUREG-2152). U. S. Nrc, 173. https://www.nrc.gov/reading-rm/doc-collections/nuregs/staff/sr2152/index.html%0Ahttps://www.nrc.gov/docs/ML1308/ML13086A202.pdf